High-Resolution X-Ray Spectroscopy of the Galactic Supernova Remnant Puppis A with the *XMM-Newton* RGS

Satoru Katsuda[1], Hiroshi Tsunemi[2], Koji Mori[3], Hiroyuki Uchida[4], Robert Petre[5], Shin'ya Yamada[1], Hiroki Akamatsu[6], Saori Konami[1,7], and Toru Tamagawa[1]

ABSTRACT

We present high-resolution X-ray spectra of cloud-shock interaction regions in the eastern and northern rims of the Galactic supernova remnant Puppis A, using the Reflection Grating Spectrometer onboard the *XMM-Newton* satellite. A number of emission lines including Kα triplets of He-like N, O, and Ne are clearly resolved for the first time. Intensity ratios of forbidden to resonance lines in the triplets are found to be higher than predictions by thermal emission models having plausible plasma parameters. The anomalous line ratios cannot be reproduced by effects of resonance scattering, recombination, or inner-shell ionization processes, but could be explained by charge-exchange emission that should arise at interfaces between the cold/warm clouds and the hot plasma. Our observations thus provide observational support for charge-exchange X-ray emission in supernova remnants.

Subject headings: atomic processes — ISM: abundances — ISM: individual objects: Puppis A — ISM: supernova remnants — X-rays: ISM

[1]RIKEN (The Institute of Physical and Chemical Research), 2-1 Hirosawa, Wako, Saitama 351-0198

[2]Department of Earth and Space Science, Graduate School of Science, Osaka University, 1-1 Machikaneyama, Toyonaka, Osaka, 60-0043, Japan

[3]Department of Applied Physics, Faculty of Engineering, University of Miyazaki, 1-1 Gakuen Kibana-dai Nishi, Miyazaki, 889-2192, Japan

[4]Department of Physics, Kyoto University, Kitashirakawa-oiwake-cho, Sakyo, Kyoto 606-8502, Japan

[5]NASA Goddard Space Flight Center, Code 662, Greenbelt MD 20771

[6]Department of Physics, Tokyo Metropolitan University, 1-1 Minami-Osawa, Hachioji, Tokyo 192-0397

[7]Department of Physics, Tokyo University of Science, 1-3 Kagurazaka, Shinjuku-ku, Tokyo 162-8601

Here, we present high-resolution X-ray spectra of the BEK/NK features using *XMM-Newton*'s Reflection Grating Spectrometer (RGS: den Herder et al. 2001). From the RGS spectra, forbidden-to-resonance line ratios in Heα triplets are found to be anomalously enhanced, especially at the BEK. We show that this anomaly could be naturally caused by the presence of CX emission.

2. Observations and Spectral Analysis

The NK and BEK were observed by *XMM-Newton* on 2003 April 17 (Obs.ID 0150150101) and 2003 May 21 (Obs.IDs 0150150201 and 0150150301), respectively, in order to obtain high-resolution spectra using the RGS instrument. The dispersion directions of the RGS are 76°.4 (NK) and 132°.3 (BEK) counterclockwise from the north, as shown in Fig. 1, which is an X-ray image of Puppis A generated from existing *XMM-Newton* and *Chandra* data. In this paper, we mainly focus on the RGS data, while we also utilize data taken by the European Photon Imaging Camera (EPIC: Turner et al. 2001; Strüder et al. 2001) to support our RGS analyses. The exposure times after removing time periods affected by soft protons are 13.5 ks and 20.8 ks for the NK and BEK, respectively. All the raw data are processed using version 11.0.0 of the XMM Science Analysis Software and the latest calibration data files available at the time of the analysis.

Since the RGS is a slitless spectrometer, off-axis sources along the dispersion direction are detected at wavelength positions shifted with respect to the on-axis source. Spatial displacement of $1'$ corresponds to a wavelength shift of 0.138 Å (or 4 eV/arcmin at 0.6 keV) for the first spectral order. Because the BEK and the NK are fairly compact ($2'$–$3'$) features with much brighter surface brightness compared to their surroundings, the RGS is capable of producing high-resolution spectra for them, with an order-of-magnitude better resolution than nondispersive CCDs. In fact, there are a number of successful RGS observations not only of moderately extended SNRs in LMC/SMC (e.g., Rasmussen et al. 2001) but also of a bright knot in the northwestern rim of SN 1006 (Vink et al. 2003).

As shown in Fig. 1, we divide the eastern RGS field of view into four sectors spaced by $0'.8$ along the cross-dispersion axis, while we extract one spectrum from the $1'.6$-width region for the north. In this way, we mitigate the photon number difference between the BEK and the NK. We smooth RGS responses originally designed for point sources, based on emission profiles along the dispersion direction with the `rgsrmfsmooth` software. For the input to the software, we arrange the X-ray images such that *Chandra* covers regions around the BEK/NK while *XMM-Newton* covers the remaining regions, and we take account of vignetting effects of *XMM-Newton*'s X-ray telescope. We generate energy-dependent RGS

the normalization ratios of O Lyγ/O Lyβ and O Lyδ/O Lyβ to 0.3 and 0.1 as are expected at kT_e ~0.5 keV (Hwang et al. 2005). We note that the kT_e values of the bremsstrahlung component are mainly determined by continuum emission above 1.5 keV. Thus, fixing ratios of Gaussian normalizations does not affect the kT_e measurements. Line centers of the most prominent 21 Gaussians are left as free parameters, while those for C Heβ and two Fe L lines (G[1] and D) are systematically shifted with respect to those of their neighboring lines (H and E). Other weak Gaussians' centers are fixed to the theoretically expected values (Smith et al. 2001). The widths of all Gaussians are fixed to zero, since significant broadening is not required from a statistical point of view. With this fitting strategy, we obtain fairly good fits for all the spectra as shown in Fig. 2. The fit results are summarized in Table 1, where we omit weak Gaussians.

The values of N_H are consistent with recent X-ray measurements (Hwang et al. 2005, 2008; Katsuda et al. 2010). The kT_e values are somewhat lower than previous results. However, prominent line intensities, which are essential for the discussion below, are not affected by the temperature difference, as the fraction of underlying continuum is very small. Line intensity ratios are generally reproduced by thermal emission models having plausible plasma parameters. On the other hand, the ratios of forbidden-to-resonance (F/R) lines in Heα triplets are apparently inconsistent with expectations of thermal emission models, as shown in Table 2. This is particularly evident for O ions in the BEK. To see if the forbidden line is stronger or the resonance line is weaker with respect to the thermal prediction inferred by other lines and continuum emission, we fit the X-ray spectra (in the E2 region) with an absorbed vpshock model (Borkowski et al. 2001), excluding the energy band of O Heα triplets. After fitting, we recover the triplet lines and find that either the intensity of the forbidden line inferred from the vpshock model is weaker than the data or the intensity of the resonance line is stronger, or both of them.

3. Discussion

We have presented high-resolution X-ray spectra of the BEK/NK features in the Galactic SNR Puppis A. The forbidden and resonance lines in the Heα triplets are clearly resolved, and their intensity ratios (F/R) are found to be generally higher than thermal predictions. This anomaly is particularly evident in the BEK, while the RGS spectrum of the NK as well as *Einstein*'s FPCS spectra of the northeastern portion (Winkler et al. 1981a,b) are more close to thermal predictions.

---

[1]We use the same labeling for Fe XVII L lines as in Gillaspy et al. (2011).

Yamaguchi et al. 2009; Uchida et al. 2012, and references therein). The recombining plasmas are characterized by strong radiative recombination continua (RRC) and enhanced $Ly\alpha/He\alpha$ ratios. We find that signatures of RRCs (i.e., strong recombination edges) are not evident in the RGS and MOS spectra in Fig. 2, although the Fe L and/or other line emission might make it difficult for us to detect such signatures. Also, the $Ly\alpha/He\alpha$ ratios for O are all around 0.6, which can be achieved by either under-ionized or equilibrium plasmas when $kT_e \gtrsim 0.2\,keV$ (Smith et al. 2001). In addition, recombination processes would enhance the Fe L lines ratio of (F+G+H)/(C+D+E) as high as >25 (Liedahl et al. 1990), which is inconsistent with our RGS measurements of 2.0±0.1 at the E2 region. Furthermore, our spectral fitting of the combined RGS and MOS spectra with a recombining plasma model (the `cie` model in SPEX: Kaastra, et al. 1996) failed to reproduce the entire X-ray spectrum; the model requires too low electron temperature to explain emission above 1 keV. These investigations indicate that the plasma here is not recombining.

Signatures of inner-shell ionization processes of Li-like ions can be found as Li-like satellite lines as well as enhanced forbidden-to-intercombination (F/I) ratio compared with collisionally excited emission (e.g., Porquet et al. 2010). In the RGS spectra, there is no indication of satellite lines, however. Also, the measured O VII F/I ratios in Table 2 marginally consistent with thermal expectations. These facts led us to consider that inner-shell ionization processes are not working efficiently in this region. We note that, whereas line emission from Li-like O is seen in the far-ultraviolet spectrum of the BEK (Blair, et al. 1995), the abundance of Li-like O would be small in the X-ray emitting region.

We then assess the feasibility of the CX scenario by calculating the expected CX flux, following Lallement (2004). The volume emissivity of CX is expressed as $P_{CX} = \sigma_{CX}\, n_H\, n_i\, V_r$. We let σ_{CX} be the CX cross section between neutral H and ions of interest, n_H the neutral H density, n_i the ion density, and V_r the relative H-ion velocity. We first consider the O VII forbidden line, so that σ_{CX} is $3.3\times10^{-15}\,cm^{-2}$ (Bodewits, et al. 2007). The value of n_H can be taken from the density of cold/warm clouds immersed in X-ray–emitting plasma, which is $\sim 50\,cm^{-3}$ (Teske & Petre 1987). The value of n_i is the density of O VIII in the hot plasma, which is $\sim 2\times10^{-4}\,cm^{-3}$ for the BEK (Hwang et al. 2008; Arendt et al. 2010). We assume that $V_r = 500\,km\,s^{-1}$, roughly the shock velocity that can produce the X-ray–emitting plasma in the BEK. These parameters give $P_{CX} \sim 1.7\times10^{-9}\,photons\,cm^{-3}\,s^{-1}$. The CX-emitting volume is calculated by the thickness of the CX layer, l_{CX}, times the interface area between the clouds and the hot plasma. The value of l_{CX} is equated to the mean free path for H-proton CX. Thus, l_{CX} is of the order of $1/\sigma n_p$, with σ being the H-proton CX cross section ($10^{-15}\,cm^{-2}$: McClure 1966) and n_p being the proton density in the plasma ($4\,cm^{-3}$: Arendt et al. 2010). Considering that only $\sim 30\%$ neutral H can charge-exchange before getting collisionally ionized (Lallement 2004) for the BEK's plasma condition, we

M82. In this context, we conclude that CX emission is a promising mechanism for explaining the anomalous F/R ratio observed in Puppis A.

One may expect to find other spectral CX signatures in addition to the Heα line ratios. However, CX spectral properties are strongly dependent on V_r and target neutrals (e.g., Beiersdorfer, et al. 2001, 2003), and investigation of CX emission is still ongoing. Therefore, further discussions call for more sophisticated CX emission modeling, which is beyond the scope of this paper and is left as future work. We also expect future observations with the non-dispersive Soft X-ray Spectrometer (SXS: Mitsuda et al. 2010) onboard the *Astro-H* satellite (Takahashi et al. 2010) to provide additional interesting information especially regarding spatial structures.

4. Conclusion

High-resolution X-ray spectra of the cloud-shock interaction regions, the BEK and the NK, in Puppis A revealed anomalous Heα triplet ratios: the O Heα F/R line ratios are found to be ~2 in the BEK. This anomalous ratio could be naturally interpreted as a result of the presence of CX emission, while resonance-scattering effects might be non-negligible as well. CX X-ray emission has been recently found in or proposed for many astrophysical sites such as comets (e.g., Lisse et al. 1996), diffuse soft X-ray background (e.g., Fujimoto et al. 2007; Ezoe et al. 2011), star-forming regions (Townsley et al. 2011a,b), and starburst galaxies (e.g., Tsuru et al. 2007; Ranalli et al. 2008; Konami et al. 2011; Liu et al. 2012). The *Astro-H*'s SXS will allow us to obtain high-resolution, spatially-resolved spectra of many more objects, shedding additional light on the role of CX processes in X-ray astrophysics.

REFERENCES

Arendt, R. G., Dwek, E., Blair, W. P., Ghavamian, P., Hwang, U., Long, K. S., Petre, R., Rho, J., & Winkler, P. F. 2010, ApJ, 725, 585

Konami, S., Matsushita, K., Tsuru, T. G., Gandhi, P., & Tamagawa, T. 2011, PASJ, 63, S913

Lallement, R. 2004, A&A, 422, 391

Liedahl, D., Kahn, S. M., Osterheld, A. L., & Goldstein, W. H. 1990, ApJ, 350, L37

Lisse, C. M., et al. 1996, Science, 274, 205

Liu, J., Mao, S., & Wang, Q. D. 2011, MNRAS, 415, L64

Liu, J., Wang, Q. D., & Mao, S. 2012, MNRAS, in press (arXiv1111.5915)

McClure, G. W. 1966, Physical Review, 148, 47

Mitsuda, K., et al. 2010, SPIE, 7732, 29

Petre, R., Kriss, G., A., Winkler, P. F., & Canizares, C. R. 1982, ApJ, 258, 22

Porquet, D., Dubau, J., & Grosso, N. 2010, Space Sci. Rev., 157, 103

Ranalli, P., Comastri, A., Origlia, L., & Maiolino, R. 2008, MNRAS, 386, 1464

Rasmussen, A. P., Behar, E., Kahn, S. M., den Herder, J. W., & van der Heyden, K. 2001, A&A, 365, L231

Reynoso, E. M., Green, A. J., Jhonston, S., Dubner; G. M., Giacani, E. B., & Goss, W. M. 2003, MNRAS, 345, 671

Read, A., M., & Ponman, T. J. 2003, A&A, 409, 395

Serlemitsos, P. J., Boldt, E. A., Holt, S. S., Ramaty, R., & Brisken, A. F. 1973, ApJ, 184, L1

Smith, R. K., Brickhouse, N. S., Liedahl, D. A., & Raymond, J. C. 2001, ApJ, 556, L91

Strüder, L., et al. 2001, A&A, 365, L18

Takahashi, T., et al. 2010, SPIE, 7732, 27

Teske, R. G., & Petre, R. 1987, ApJ, 314, 673

Townsley, L., et al. 2011a, ApJS, 194, 15

Townsley, L., Broos, P. S., Chu, Y-H.; Gruendl, R. A., Oey, M. S., & Pittard, J. M. 2011b, ApJS, 194, 16

Table 1. Spectral-fit parameters

Component	Parameter	Region				
		E1	E2	E3	E4	N
Absorption	N_{H} (10^{21} cm^{-2})	2.70±0.01	2.80±0.01	2.80±0.01	2.85±0.01	2.58±0.01
Bremsstrahlung	kT_e (keV)	0.32±0.01	0.31±0.01	0.33±0.01	0.32±0.01	0.30±0.01
	Normalization[a]	5264±93	9124±133	6744±117	7808±117	5397±90
Gaussian: C Lyα+Si L+S L	Center (eV)	$366.8^{+0.2}_{-0.1}$	$367.2^{+0.2}_{-0.1}$	$366.7^{+0.4}_{-0.3}$	$365.4^{+0.4}_{-0.3}$	$367.4^{+0.3}_{-0.8}$
	Normalization[a]	822±80	1486±118	1257±139	1723±139	380±52
N Heα (f)	Center (eV)	$419.2^{+0.2}_{-0.5}$	419.2±0.3	418.4±0.5	419.7±0.5	$420.5^{+0.8}_{-0.6}$
	Normalization[a]	100±18	201±26	145±26	243±33	82±16
N Heα (r)	Center (eV)	$429.7^{+0.3}_{-0.2}$	$430.1^{+0.3}_{-0.2}$	429.9±0.5	429.7±0.5	430.6±0.5
	Normalization[a]	146±17	223±24	169±23	199±27	72±15
C Lyβ	Center (eV)	$434.9^{+0.7}_{-0.2}$	$435.1^{+0.6}_{-0.3}$	$435.2^{+0.7}_{-0.6}$	$434.7^{+0.7}_{-0.6}$	$435.2^{+0.7}_{-0.6}$
	Normalization[a]	60±14	87±18	55±18	87±22	51±13
C Lyγ	Center (eV)	459[b]	459[b]	459[b]	459[b]	459[b]
	Normalization[a]	25±8	31±10	24±10	14±8	< 8
N Lyα+Heβ	Center (eV)	499.4±0.2	$500.2^{+0}_{-0.2}$	$499.8^{+0.2}_{-0.3}$	$499.6^{+0.2}_{-0.3}$	$499.6^{+0.5}_{-0.4}$
	Normalization[a]	143±9	254±13	222±12	252±14	162±11
O Heα (f)	Center (eV)	$559.8^{+0.4}_{-0.1}$	560.7±0.1	560.5±0.5	560.2±0.5	561.2±0.2
	Normalization[a]	705±27	1167±36	1042±36	1119±38	417±23
O Heα (i)	Center (eV)	$566.8^{+1.0}_{-0.9}$	$568.3^{+0.3}_{-1.1}$	$570.7^{+0.4}_{-0.7}$	$568.5^{+0.4}_{-0.7}$	$567.5^{+0.4}_{-1.1}$
	Normalization[a]	107±24	190±30	298±31	255±34	168±22
O Heα (r)	Center (eV)	573.1±0.2	$574.1^{+0.3}_{-0.2}$	573.4±0.1	572.9±0.1	$574.3^{+0.2}_{-0.3}$
	Normalization[a]	601±25	771±30	527±31	646±33	492±21
O Lyα	Center (eV)	$652.7^{+0.5}_{-0.1}$	653.4±0.2	653.0±0.2	652.8±0.2	653.4±0.4
	Normalization[a]	979±38	1223±47	1154±46	1329±51	631±36
O Heβ	Center (eV)	664.4±0.8	$665.0^{+0.3}_{-0.7}$	$665.4^{+1.3}_{-1.4}$	$666.0^{+1.3}_{-1.4}$	667.0±1
	Normalization[a]	161±24	285±29	197±27	136±29	110±17
O Heγ	Center (eV)	$699.0^{+0.9}_{-0.8}$	700.7±0.6	$698.9^{+1.1}_{-0.8}$	$698.2^{+1.1}_{-0.8}$	700.7±1.1
	Normalization[a]	68±8	74±10	65±11	74±13	42±9
Fe L (G+H)	Center[c] (eV)	$724.9^{+0.4}_{-0.1}$	$725.1^{+0.2}_{-0.4}$	$724.9^{+0.1}_{-0.3}$	$725.2^{+0.1}_{-0.3}$	$725.2^{+0.1}_{-0.4}$
	Normalization[a]	247^{+16}_{-15}	362^{+21}_{-20}	331^{+19}_{-18}	332^{+20}_{-19}	156^{+13}_{-12}
Fe L (F)	Center (eV)	$739.3^{+0.8}_{-0.5}$	$738.5^{+0.1}_{-0.7}$	$739.3^{+0.9}_{-0.3}$	$738.1^{+0.9}_{-0.3}$	$738.9^{+0.8}_{-0.3}$
	Normalization[a]	89±11	156±13	94±12	99±12	65±8
O Lyβ	Center (eV)	$773.5^{+0.2}_{-0.6}$	773.8±0.3	$773.3^{+0.4}_{-0.6}$	$772.9^{+0.4}_{-0.6}$	773.7±0.5
	Normalization[a]	151±7	187±8	160±7	169±8	97±6
Fe L (D+E)	Center[c] (eV)	810.6±0.8	810.1±0.2	810.0±0.4	810.0±0.4	810.1±0.7
	Normalization[a]	74^{+10}_{-9}	110^{+11}_{-10}	98^{+11}_{-10}	90^{+11}_{-10}	50^{+7}_{-6}
Fe L (C)	Center (eV)	$826.6^{+0.4}_{-1.0}$	826.1±0.5	825.6±0.5	826.1±0.5	$826.2^{+0.3}_{-0.6}$
	Normalization[a]	105±6	173±0.8	135±7	152±8	78±5
Ne Heα (f)+Fe L	Center (eV)	902.0±0.6	$903.3^{+0.5}_{-0.2}$	$902.6^{+0.4}_{-0.2}$	$902.6^{+0.4}_{-0.2}$	$903.5^{+0.6}_{-0.4}$
	Normalization[a]	122±6	185±7	156±6	175±7	75±4
Ne Heα (r)+Fe L	Center (eV)	$921.2^{+0.3}_{-0.5}$	$921.6^{+0.1}_{-0.3}$	$921.2^{+0.3}_{-0.4}$	$921.8^{+0.3}_{-0.4}$	922.4±0.2
	Normalization[a]	141±6	224±7	168±6	188±7	111±5
Ne Lyα+Fe L	Center (eV)	$1023.6^{+1.2}_{-1.4}$	$1022.5^{+0.5}_{-1.2}$	$1020.5^{+0.2}_{-1.4}$	$1022.1^{+0.2}_{-1.4}$	$1020.4^{+1.1}_{-0.8}$
	Normalization[a]	83±5	97±6	96±5	102±6	35±3
χ^2/d.o.f.		1423/968	1740/1151	1698/1114	1664/1181	949/612

Note. — [a] In units of 10^{-4} photons cm^{-2} s^{-1}.
[b] Fixed values.
[c] Line centers of H and E are shown, while those of G and D are systematically shifted by +2 eV from H and E, respectively.
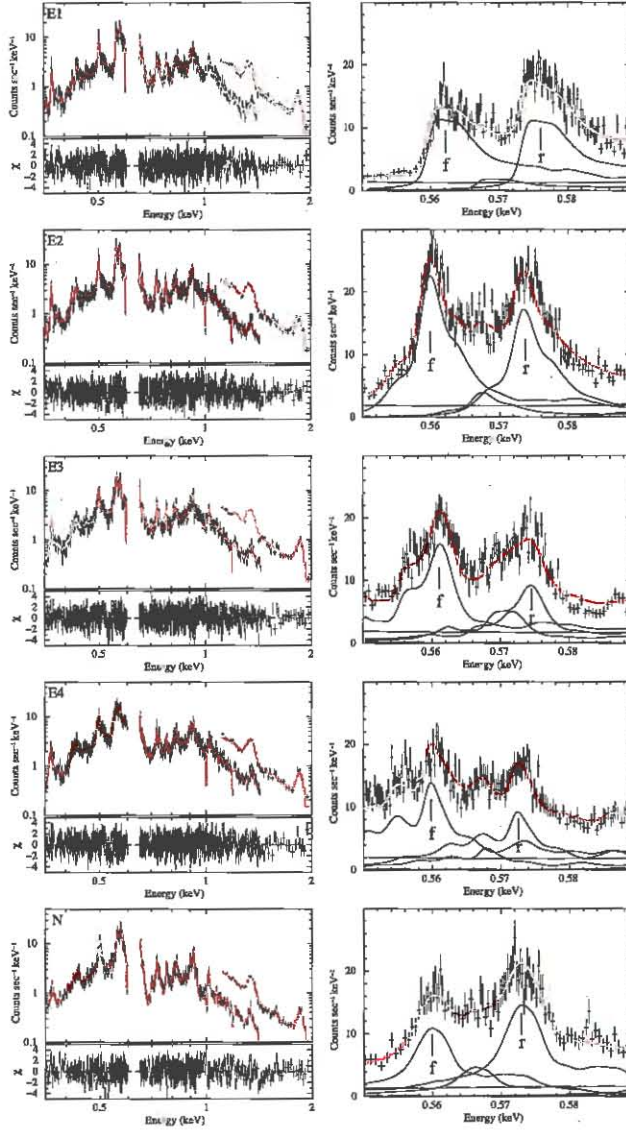
Fig. 2.— *XMM-Newton* spectra of the five regions in Fig. 1. The data covering below 0.6 keV, 0.65–1.5 keV, and above 1.1 keV are the first order RGS1+2, the second order RGS1+2, and MOS1+2, respectively. These data are simultaneously fitted with a phenomenological model (see text), and the best-fit models are shown in red. Lower panels show the residuals. The insets show close-up spectra for O Heα triplets with individual best-fit model components.